Energy & Environmental Science

PAPER

View Article Online
View Journal | View Issue

CrossMark click for updates

Cite this: *Energy Environ. Sci.*, 2014, **7**, 3747

On rechargeability and reaction kinetics of sodium–air batteries†

Hossein Yadegari,[a] Yongliang Li,[a] Mohammad Norouzi Banis,[a] Xifei Li,[a] Biqiong Wang,[a] Qian Sun,[a] Ruying Li,[a] Tsun-Kong Sham,[b] Xiaoyu Cui[c] and Xueliang Sun*[a]

Received 28th May 2014
Accepted 18th August 2014

DOI: 10.1039/c4ee01654h

www.rsc.org/ees

Rechargeable metal–air batteries are widely considered as the next generation high energy density electrochemical storage devices. The performance and rechargeability of these metal–air cells are highly dependent on the positive electrode material, where oxygen reduction and evolution reactions take place. Here, for the first time, we provide a detailed account of the kinetics and rechargeability of sodium–air batteries through a series of carefully designed tests on a treated commercial carbon material. Surface area and porous structure of the positive electrode material were controlled in order to gain detailed information about the reaction kinetics of sodium–air batteries. The results indicate that discharge capacity is linearly correlated with surface area while morphology of the solid discharge product is strongly dependent on specific surface area and pore size. Furthermore, it was found that the chemical composition of discharge products as well as charging overpotential is affected by discharge reaction rate.

Border context

Metal–air batteries, which employ conversion chemistry rather than intercalation phenomena, can compete with gasoline in terms of theoretical energy density. Among different metal–air systems, Li–air batteries have received enormous amounts of attention over the past few years. However, Li–air cells still suffer from high charging overpotential which decreases the energy efficiency of the cell. As an alternative Li–air system, Na–air has been considered recently in which lithium metal is replaced by sodium. Compared with Li–air, the Na–air battery system has lower charging overpotential which fits in the electrochemical stability window of available electrolytes and may result in higher cycling performance. However, an accurate understanding behind the chemistry of the cell is the key to achieve a reversible battery system which has not been addressed. The chemistry of the Na–air cell is investigated in the present study. Electrode materials used in this study are prepared by a simple heat-treatment procedure under various corrosive atmospheres using non-precious carbon black as starting materials. Heat-treatment of carbon black enables a precise control over the surface area and porosity of the air electrode material. The correlation between discharge capacity, surface area and porosity of the cathode materials is also studied in detail.

1. Introduction

The widespread use of fossil fuels in the past few decades has resulted in a substantial increase of greenhouse gas concentrations and has been a prime contributor to the serious issue of global warming. Since fossil fuels are predominantly consumed for transportation purposes, a switch from the conventional internal combustion engines (ICEs) to electric vehicles (EVs) has received enormous consideration.[1] Furthermore, electric engines have higher conversion efficiency than ICEs thus making them even more attractive.[1] Lithium-ion batteries (LIBs) have been the technology of choice for application in EVs due to their relatively high volumetric and gravimetric energy density as well as longer battery cycle life in comparison with other available battery systems.[2] However, current LIB-EVs are restricted to low-mileage applications as a result of limited specific energy density, long charge time as well as high cost.[1–3]

Metal–air cells, which use a chemistry different from intercalating LIBs, have theoretical specific energy densities high enough to compete with gasoline.[1,4] The high specific energy densities seen for metal–air batteries are related to the use of high energy alkaline metals as anodes and oxygen, from ambient air, as cathode materials. Using light metal elements, such as lithium, as the anode material to form a lithium–air (Li–air) battery system has attracted a great deal of attention.[5–7] However, large charge overpotentials in these batteries limit their cycle life to less than 100 cycles.[8] A recently considered

[a]*Department of Mechanical and Materials Engineering, University of Western Ontario, London, Ontario N6A 5B9, Canada. E-mail: xsun@eng.uwo.ca*

[b]*Department of Chemistry, University of Western Ontario, London, Ontario N6A 5B7, Canada*

[c]*Canadian Light Source, Saskatoon S7N 0X4, Canada*

† Electronic supplementary information (ESI) available: Extended characterization results, including electrochemical data, SEM micrographs, XRD and XPS data. See DOI: 10.1039/c4ee01654h

alternative metal–air battery is the sodium–air (Na–air) battery, in which lithium is replaced by sodium metal.[9–13] Na–air battery systems have a lower theoretical specific energy density (1605 or 1108 W h kg^{-1} considering Na_2O_2 or NaO_2 as discharge products, respectively) compared to Li–air battery systems. However, Na–air batteries also demonstrate lower charge overpotential which may result in better cyclic performance.[9]

Only a few studies address the Na–air battery system[9–18] with only a limited understanding behind the chemistry of the cell. For instance, various sodium oxides have been reported as discharge products of the Na–air battery system. Fu *et al.*[9,10] have investigated Na–air cells with carbonate and ether based electrolytes while different carbon materials were used as the air electrode. Based on selected area electron diffraction (SAED), their results report the production of sodium peroxide (Na_2O_2) as a discharge product with the use of either carbonate or ether electrolytes. At the same time, different charge–discharge mechanisms with various discharge products are proposed by Kim *et al.*[11] using carbonate and ether based electrolytes. In this study sodium carbonate and hydrated sodium peroxide were produced as discharge products using carbonate and ether based electrolytes, respectively. More recently, sodium superoxide (NaO_2) has also been shown to be the discharge product of the Na–air battery systems with the use of an ether based electrolyte.[12,13] In addition, the same research group investigated the electrochemistry and thermodynamic of the Na–air cell in a series of systematic studies in which sodium superoxide was the major discharge product.[14,15] McCloskey *et al.* also studied the chemical and electrochemical differences of the Na– and Li–air cells and found "cleaner" chemistry in the case of the Na–air cell with a lower amount of parasitic products during the charge cycle of the cell.[17] The lower amount of decomposition products and hence lower charging overpotential in the Na–air cell are related to the more stability of NaO_2 compared to Li_2O_2, the major discharge products of Na– and Li–air cells, respectively.[17] Meanwhile, Ceder's research group showed using theoretical calculations that Na_2O_2 is the stable phase in the bulk form and NaO_2 is only more stable at the nanoscale below 10 nm in particle size.[18] Based on the aforementioned studies, it can be concluded that kinetic factors play a significant role in Na–air cells, resulting in the formation of different phases of sodium oxides at various studies.

Even though sodium and lithium share many physicochemical properties, the chemistry of the Li–air and Na–air cells is not the same. While sodium forms stable sodium superoxide, lithium superoxide is thermodynamically unstable.[9] Therefore, it is expected that both sodium peroxide and superoxide would be formed under different physicochemical environments, however kinetic factors may stabilize a certain phase over the other oxide. In the present study, we show that the morphology and chemical composition of the discharge products in the Na–air battery system depend on various factors including current density and air electrode materials. In addition, charge performance of the Na–air system can be controlled by manipulating the discharge products.

2. Results and discussion

The gas diffusion electrode serves as a diffusing medium for the positive active material (oxygen) in metal–air batteries, as well as a substrate for the accumulation of discharge products, thus making the final electrochemical performance of the metal–air system strongly dependent on the efficiency of the air electrode. The gas diffusion electrode material used in this work was prepared *via* heat-treatment of carbon black under various corrosive atmospheres, as outlined in Fig. 1a. Using the heat-treated carbon materials enables the precise control over the porosity and surface area of the air electrode materials. This heated-treated carbon material based on commercially used carbon black with the post-treatments has been intensively used in various systems such as fuel cells and high energy batteries.[19–21] The heat-treated carbon materials allow us to understand correlations between discharge capacity, surface area and porosity of the cathode materials. Carbon black is primarily composed of graphitic crystallites bound together by disordered carbon.[22] Heat-treatment of carbon black removes disordered carbon, resulting in a highly porous structure. Micropore boundaries grow with increasing treatment time and eventually result in the formation of mesopores.[22] Initially, as the treatment time increases, the number of mesopores with a

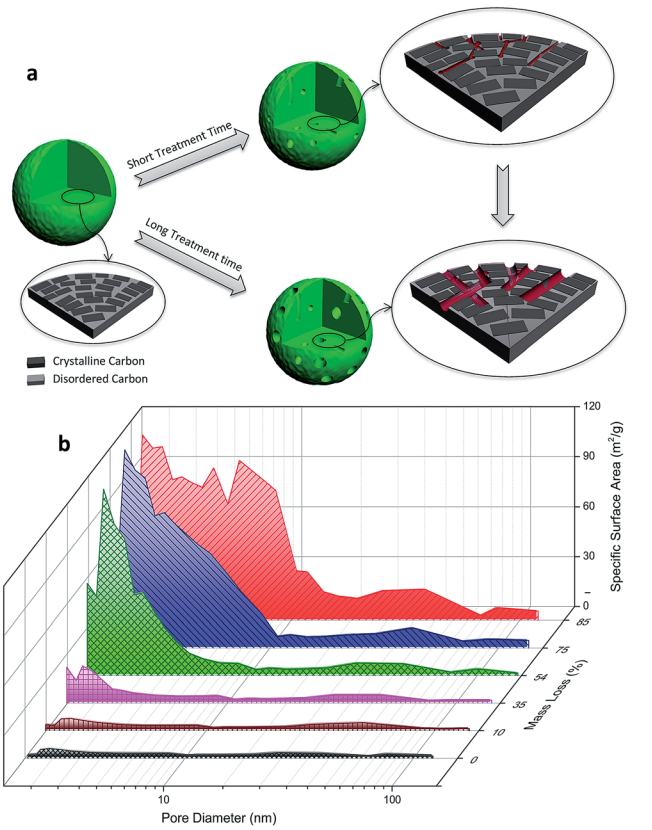

Fig. 1 Schematic diagram of the carbon black electrode material during the heat-treatment process (a); pore size distribution plot for NH_3-treated carbon materials with different mass losses from 0 to 85% (b).

size of less than 10 nm increases while a further treatment results in an increase of pore volume. As a result, heat-treated carbons with higher mass losses demonstrate elevated specific surface area values, higher edge to surface ratios, and larger pore size.[19] Nitrogen adsorption/desorption measurements were carried out to illustrate the surface porosity characteristics. The nitrogen adsorption isotherms of the pristine carbon (N330) and heat-treated carbon material under different atmospheres and with various mass losses are shown in ESI Fig. S1.† The pristine N330 carbon presents the isotherm of type II, while for heat-treated carbons the type of isotherm is gradually changing from type II to type IV with the increase of mass loss. In addition, the nitrogen adsorption ability of heat-treated carbon is also considerably increasing with the increase of mass loss, indicating the increase of the active surface area. The pore size distributions and pore volumes of the carbon materials were obtained from the Barrett, Joyner, and Halenda (BJH) analysis using the adsorption branch of each isotherm.

Pore size distribution of the NH_3-treated carbon material is plotted against mass loss, and presented in Fig. 1b (similar data for CO_2 and CO_2/H_2-treated carbons are shown in ESI Fig. S2†). Heat-treatment of carbon materials under NH_3, CO_2, and CO_2/H_2 atmospheres results in a considerable increase of specific surface area in the range of mesopores less than 10 nm (see also ESI Table S1†). The advantage of using heat-treated carbon materials is that various morphologies, surface areas and functional groups can be produced by simply altering pretreatment parameters.

As-prepared carbon materials were tested as gas diffusion electrodes for Na–air cells. Fig. 2a shows the discharge curves of different NH_3-treated carbon samples. All treated carbon materials indicate a flat discharge plateau at 2.2 V, delivering increasing specific discharge capacity with an increase in mass loss (see also Fig. 2b). The plot of specific surface area of the treated carbon material as a function of mass loss percentage indicates that specific discharge capacity increases with specific surface area, as shown in Fig. 2b. Specific discharge capacity values increase quantitatively from 505 to 2783 mA h g^{-1} with a mass loss increase of 10 to 85%. In fact, a higher surface area presents a greater density of accumulation sites for deposition of solid discharge products, resulting in an increase of the specific discharge capacity of the cell. In addition, a highly porous air electrode structure results in a greater diffusion path for both oxygen and sodium species, causing decreased mass transfer resistance, and increased cell capacity by postponing the potential drop. Similar trends were also observed for CO_2 and CO_2/H_2 treated carbon materials (ESI Fig. S3†). The specific discharge capacity per actual surface area (calculated based on the specific discharge capacity (mA h g^{-1}) and the specific surface area of the corresponding electrode (m^{-2} g^{-1})) of the electrode materials was plotted as a function of mass loss percentage, as shown in Fig. 2c. Apart from the original N330 sample, all other treated carbon materials demonstrated a constant specific capacity per surface area. These constant values for different treated carbon materials illustrate the substantial effect of surface area on specific capacity for the Na–air battery system. In other words, actual surface area resulting

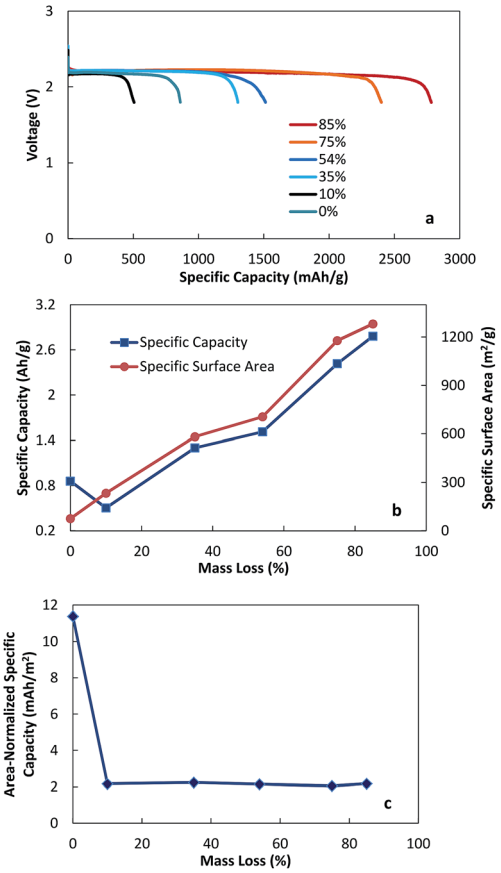

Fig. 2 Discharge curves of Na–air cells using NH_3-treated carbon materials with different mass losses from 0 to 85% as cathode electrodes recorded at a current density of 75 mA g^{-1} (a); plot of specific capacitance and specific surface area of the cathode electrode materials of the cells depicted in (a) as a function of mass loss (b); area-normalized specific capacity of the cells depicted in (a) as a function of mass loss (c).

from mesopores of the electrode materials dominantly determines the specific capacity of the air electrode. It should also be noted that the nature of porosity for pristine carbon black is different from other treated carbon materials;[19,20] the porosity of pristine carbon black originates from pores that exist between carbon particles, and have an average size of 30 nm. The porosity of treated carbon materials, however, stems from mesopores produced during the heat-treatment process and is chemically different in nature. Furthermore, heat-treatment of carbon also results in the creation of small pores in the micropore region. Although these micropores increase the BET surface area, they are not accessible by the electrolyte and hence oxygen diffusion into these micropores is restricted. Therefore, pristine carbon demonstrates higher area-normalized specific capacity compared with heat-treated carbon materials. The total pore volume of heat-treated carbons is also plotted as a function of mass loss and shown in ESI Fig. S4.† Although the total pore volume of heat-treated carbons also shows a growing trend, it does not show a direct correlation with specific capacity in the Na–air cell.

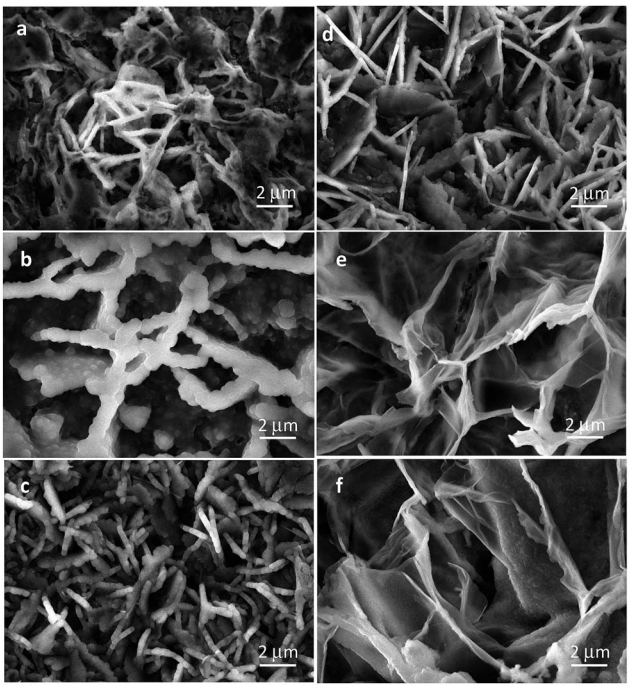

Fig. 3 Morphology of discharge products of the Na–air cells using different NH_3-treated carbon materials with 0 (a), 13 (b), 35 (c), 50 (d), 75 (e) and 85% (f) mass losses as cathode electrodes (discharge current density: 75 mA g^{-1}).

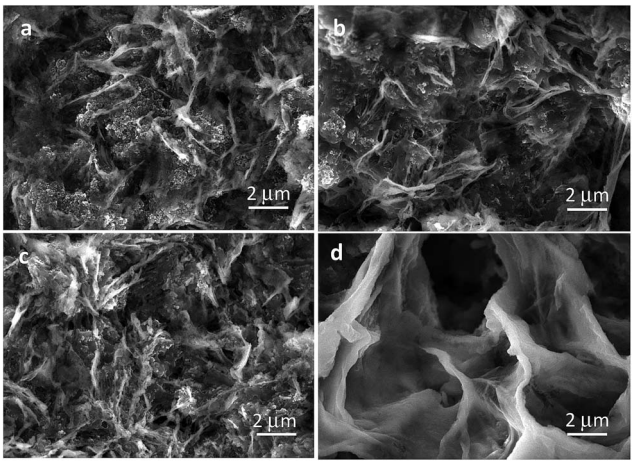

Fig. 4 Morphology of discharge products of the Na–air cell using a NH_3-treated carbon material with 85% mass loss as a cathode electrode after 8 (a), 16 (b), 24 (c) and 36 (d) hours of discharge (discharge current density: 75 mA g^{-1}).

The morphology of discharge products is another crucial factor that influences the discharge properties of metal–air systems, as well as the charge characteristic and performance of the cell.[23–26] Fig. 3a–f display SEM micrographs of discharge products for the carbon material under various durations of NH_3 treatment. The discharge products observed for pristine carbon black display rod-shaped particles which are stacked upon each other (Fig. 3a). The rod-shaped particles can also be observed in the case of NH_3-treated carbons with a mass loss of 10–54%. However, as the mass loss increases, the dimension of discharge products shrinks and gradually transforms from rod-shaped particles to a thin film structure with a thickness of a few nanometers. The discharge products of treated carbon samples with an elevated mass loss (Fig. 3e and f) predominantly exist as ultrathin nanosheets, uniformly covering the carbon surface. The same morphological changes were also observed for samples treated with CO_2 and CO_2/H_2 (ESI Fig. S5 and S6†). SEM images of initial and charged NH_3-treated carbon electrodes are also shown in ESI Fig. S7† for comparison purposes.

To identify the growth mechanism for the produced nanosheets, morphological changes were observed at different depths of discharge for treated carbon samples with 85% mass loss. The morphologies of discharge products after 8, 16, 24 and 36 hours of discharge are depicted in Fig. 4. Tiny separated fibrils of the solid discharge product can be observed after 8 hours of discharge (Fig. 4a), while a major part of the carbon surface is left uncovered. After 16 hours of discharge the initial fibrils increase in size and begin to partially connect with one another in the form of island-shaped structures (Fig. 4b). The same morphology can be observed after 24 hours of discharge, but to a greater extent with a greater degree of connection between the formed islands. Following 36 hours of discharge, the carbon surface is totally covered with a uniform wrinkled film of discharge product (Fig. 4d). The thin layer is composed of interconnected primary discharge particles. More SEM micrographs with various magnifications of the positive electrode after multiple steps of discharge process are also shown in ESI Fig. S8.†

The morphology of discharge products can be specified by the equilibrium between nucleation and growth rate. Greater density of nucleation sites, as seen with higher surface area materials, will result in smaller-sized particles being produced. However, lower surface area materials have limited nucleation sites, resulting in the formation of larger-sized particles. Recently, an *in situ* AFM study by Wen *et al.*[26] on the Li–O_2 electrochemical reaction mechanism revealed that the nucleation process of discharge product (Li_2O_2) mainly occurs at step edges of the carbon substrate due to the higher surface energy at these locations. The same mechanism is likely to be responsible for different morphologies of discharge products in the Na–air cells. Heat-treatment of carbon materials under corrosive conditions results in the production of new pores, inevitably leading to an increase in edge/plate ratio. The edge plane carbon sites serve as nucleation points for discharge products due to elevated electron transfer reactions occurring at these locations compared to the basal carbon plane.[27] As a result, the nucleation rate outpaces the growth rate on the carbon materials with longer treatment time as a consequence of greater edge sites, leading to the dominant production of a film-like structure. The proposed mechanism for discharge product formation is schematically illustrated in Fig. 5. The control of discharge product morphology is critical in rechargeable metal–oxygen battery systems. It is paramount for the produced discharge product to revert back into the starting

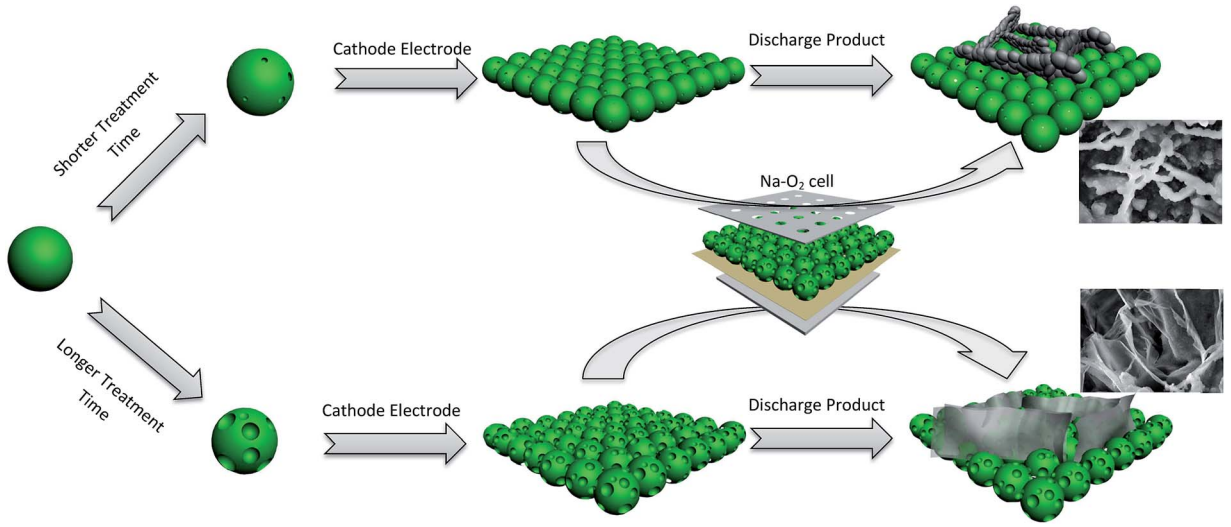

Fig. 5 Schematic diagram of the Na–air cell using different heat-treated carbon materials as cathode electrodes.

materials in order for the cell to be considered rechargeable. Solid discharge products larger in size have greater charging overpotential due to their limited interaction with the substrate. In addition, charging overpotential has a smaller value at the substrate/discharge product interface (which is accessible by the electrolyte) compared to the bulk of products. Therefore, the decomposition process begins at these interfaces. Progression of the decomposition process at interface sites hereupon cuts off the electrical contact to the remaining discharge particles and prevents them from entirely revert back, leading to a limited cycling performance, as reported by Hartmann *et al.*[13] However, a uniform thin layer of discharge product may result in an enhanced charging process by increasing the interaction between the substrate and discharge product.

To investigate the charging performance of the electrode materials, NH_3-treated carbon materials with 85% mass loss were subjected to discharge down to a specific capacity of 1.0 Ah g^{-1} and then subsequently charged back at a current density of 75 and 40 mA g^{-1}, respectively, as outlined in Fig. 6a. Three distinct charge regions with a potential range of 2.3–2.75 (region I), 2.75–3.4 (region II) and 3.4–3.9 V (region III) can be distinguished during the charge process. These three charge potential regions will be referred to as lower, middle and higher potentials, respectively. Similar charge profiles were observed for CO_2 and CO_2/H_2 treated carbon materials as well (ESI Fig. S9†). Based on the thermodynamic standard potentials of different sodium oxides ($E_{Na_2O}^0 = 1.95$, $E_{Na_2O_2}^0 = 2.33$ and $E_{NaO_2}^0 = 2.27$ V)[12] and considering the discharge voltage of the cell (Fig. 2a), the most probable discharge product for the Na–air system is either sodium peroxide (Na_2O_2) and/or sodium superoxide (NaO_2). Both of these oxides have been previously reported as major products for Na–air battery systems.[9–17] However during charging three notable steps are observed, as shown in Fig. 6a, indicating that the charge reaction is not a simple one-species decomposition reaction but rather the formation of multiple initial products produced during discharge.

To better understand the chemistry of Na–air batteries, the discharge product of the Na–air cell was examined by the X-ray diffraction (XRD) technique. The recorded patterns were obtained from air electrode materials before and after discharge to 1.8 V and are depicted in Fig. 6b. The XRD confirms the existence of multiple discharge products. However, the major discharge product correlates well with hydrated sodium peroxide ($Na_2O_2 \cdot 2H_2O$, JCPDS reference card no. 015-0064), as opposed to the expected sodium peroxide. The minor peaks found in the spectrum can be associated with sodium superoxide (NaO_2, JCPDS reference card no. 006-0500). The presence of hydrated sodium peroxide as a discharge product of the Na–air cells using an ether (TEGDME) based electrolyte has been previously reported by Kim *et al.*[11] and more recently by Jian *et al.*[16] Kim *et al.* have also proposed a reaction mechanism in which TEGDME was subjected to the reaction with superoxide ions to produce carbon dioxide and water. However, Nazar *et al.*[25] previously reported in a systematic study on Li–air cell chemistry that TEGDME does not significantly undergo decomposition in the presence of superoxide ions. However, PVDF readily reacts with this ion and produces hydrogen peroxide.[25] In the case of the Na–air battery system sodium superoxide can react with hydrogen peroxide to produce hydrated sodium peroxide. Thus, the following mechanism can be adopted for the positive electrode in Na–air cells. Discharge reactions of the Na–air cell at the positive electrode can be proposed as follows:

$$Na^+ + O_2 + e^- \rightarrow NaO_2 \quad (1)$$

$$2Na^+ + O_2 + 2e^- \rightarrow Na_2O_2 \quad (2)$$

Furthermore, the following side reactions may also occur:

$$O_2^- + -(CH_2-CF_2)- \rightarrow H_2O_2 + O_2 + -(CH{=}CF)- + F^- \quad (3)$$

$$NaO_2 + Na^+ + 2H_2O_2 \rightarrow Na_2O_2 \cdot 2H_2O + O_2 \quad (4)$$

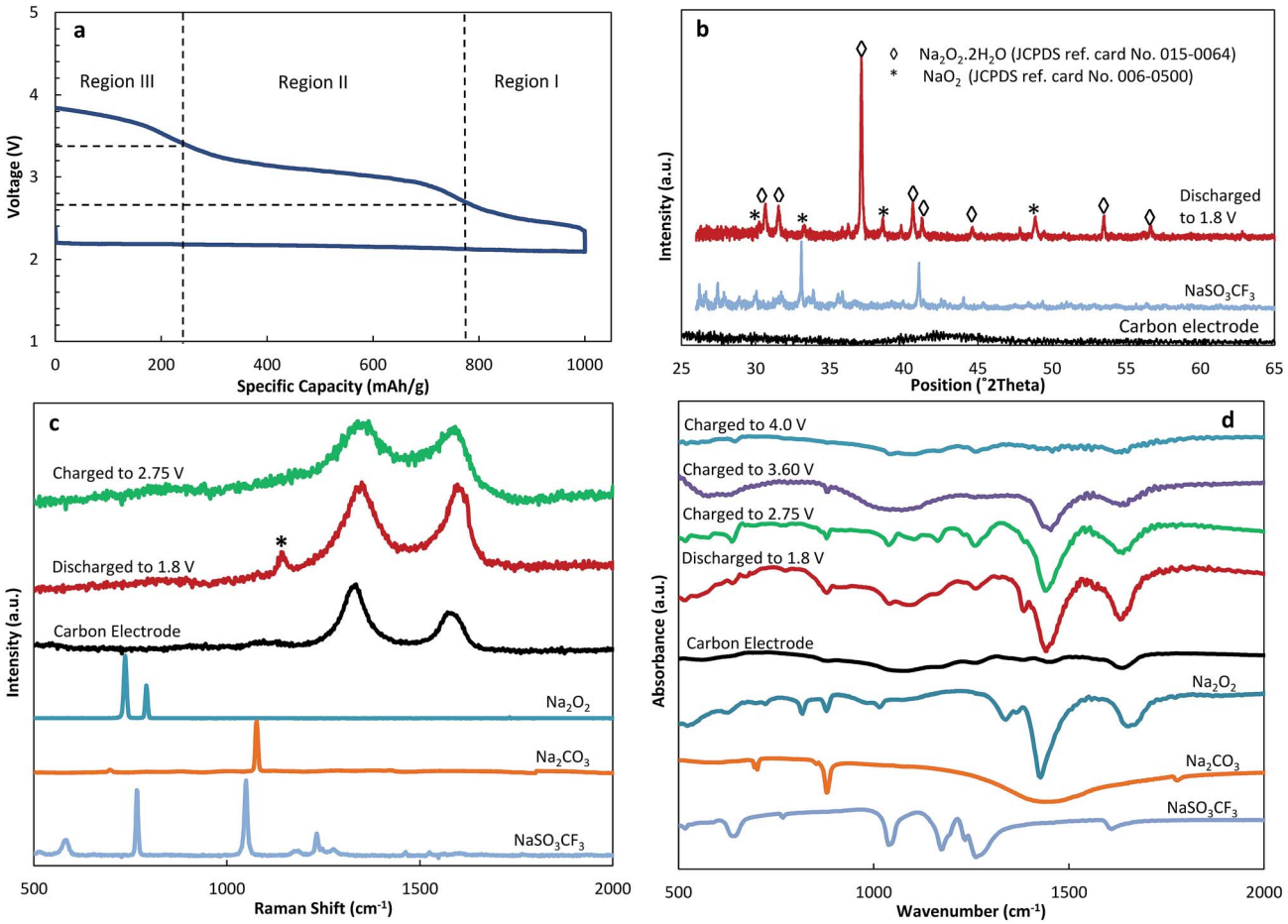

Fig. 6 Limited discharge and charge curves of the Na–air cell using a NH_3-treated carbon material with 85% mass loss at current densities of 75 and 40 mA g^{-1}, respectively (a); XRD patterns of positive electrode, electrolyte salt and discharge products of the Na–air cell shown in panel a (b); Raman spectra of the positive electrode after discharge and first charge step shown in panel a, the peak marked with an asterisk refers to the NaO_2 phase[28] (c); FTIR spectra of the positive electrode after discharge and charge to the various regions shown in panel a (d).

$$Na_2O_2 + 2H_2O_2 \rightarrow Na_2O_2{\cdot}2H_2O + O_2 \quad (5)$$

In addition, XRD patterns of the positive electrode after charging the cell to 2.75, 3.60 and 4.0 V (corresponding to the various charging steps indicated in Fig. 6a) are shown in ESI Fig. S10.† The peaks related to the NaO_2 phase disappeared after charging the cell to 2.75 V, indicating that the decomposition of NaO_2 takes place at the region I of the charge cycle. Charging the cell to 3.6 and 4.0 V results in the degradation of peaks related to the Na_2O_2 phase.

Further, discharge products of the Na–air cell after discharge and charge to different potentials (shown in Fig 6a) were also examined by Raman spectroscopy. The resultant spectra combined with reference $NaSO_3CF_3$, Na_2O_2 and Na_2CO_3 for comparison purposes are depicted in Fig. 6c. The spectra obtained from the positive carbon electrode show two characteristic D and G bands related to the disordered and graphitic carbons, respectively. An additional peak at 1141 cm^{-1} appeared after discharge of the cell to 1.8 V is related to the NaO_2 phase[28] that disappeared after charging the cell to 2.75 V. No Raman peak associating with the Na_2O_2 phase was detected, probably due to its weaker Raman signal. Raman and IR spectroscopies are complementary analytical techniques, since transitions allowed in Raman may be forbidden in IR or *vice versa*. As a result, the compound with weak Raman signal may show strong absorbance in IR. Accordingly, FTIR spectra of the positive electrode at different electrochemical states were also recorded, as shown in Fig. 6d. Comparison of FTIR spectra of electrode materials before and after discharge to 1.8 V reveals a characteristic peak at 879 and 1442 cm^{-1}, respectively, attributed to Na_2O_2, providing further evidence as to the production of sodium peroxide during discharge.[29] It should also be noted that NaO_2 does not show any characteristic peak in IR due to the homopolar nature of the superoxide ion.[29] In addition, the Na_2O_2 characteristic peaks remained in the spectra until charging the cell to 4.0 V (corresponding to the region III of Fig. 6a). Based on XRD, Raman and FTIR results, it can be concluded that the charge plateau at lower (region I) and higher (region III) potentials is related to the decomposition reactions of NaO_2 and Na_2O_2, respectively (see also Fig. 6a). However, a deeper understanding about the discharge product of the Na–air cell is required to figure out the nature of other charge plateau at middle (region II) potentials.

The formation of superoxide ions is a result of a single electron transfer process resulting in the formation of NaO_2 being kinetically more favorable, while Na_2O_2 is thermodynamically more stable than NaO_2 ($\Delta G_f^0{}_{Na_2O_2} = -449.7$ kJ mol^{-1}; $\Delta G_f^0{}_{NaO_2} = -218.8$ kJ mol^{-1}).[12,15] Accordingly, the chemical composition of the discharge product would change under various discharge conditions. To examine this hypothesis, Na–air cells were discharged at different current densities and then charged back under a constant current density. Discharge curves of Na–air cells obtained at different current densities from 75 to 300 mA g^{-1} are depicted in Fig. 7a. As the discharge current density increases, the discharge voltage and specific discharge capacity decrease slightly. Furthermore, the discharge curve obtained at a current density of 75 mA g^{-1} indicates a flat plateau situated at 2.2 V. However, the discharge curve recorded at a current density of 150 mA g^{-1} shows an initial plateau at around 2.2 V with an additional sloping region at 2.0 V. Similar behavior can also be observed for the discharge curve obtained at a current density of 300 mA g^{-1}, except for lower discharge voltages mainly because of charge and mass transfer resistances. Based on the standard equilibrium potentials of sodium oxide species, the first (higher potential) and second (lower potential) discharge plateaus can be respectively attributed to the formation of Na_2O_2 and NaO_2. In addition, a relatively large change can be observed between the discharge capacity for cells discharged at current densities of 75 and 150 mA g^{-1} (compared with the cell discharged at 300 mA g^{-1}), which can be attributed to the difference between the number of electrons exchanged in eqn (1) and (2).

X-ray photoelectron spectroscopy (XPS) analysis was employed to further identify the chemical composition of discharge products at different current densities. Because of the high sensitivity of XPS in analytical speciation measurements, it is chosen to study the chemical composition of discharge products at different current densities. The XPS results for O1s of reference sodium peroxide and discharge products of the cells discharged at current densities of 75 and 300 mA g^{-1} are depicted in Fig. 8. The spectrum of reference sodium peroxide demonstrates one peak at 530.9 eV related to the peroxide ion

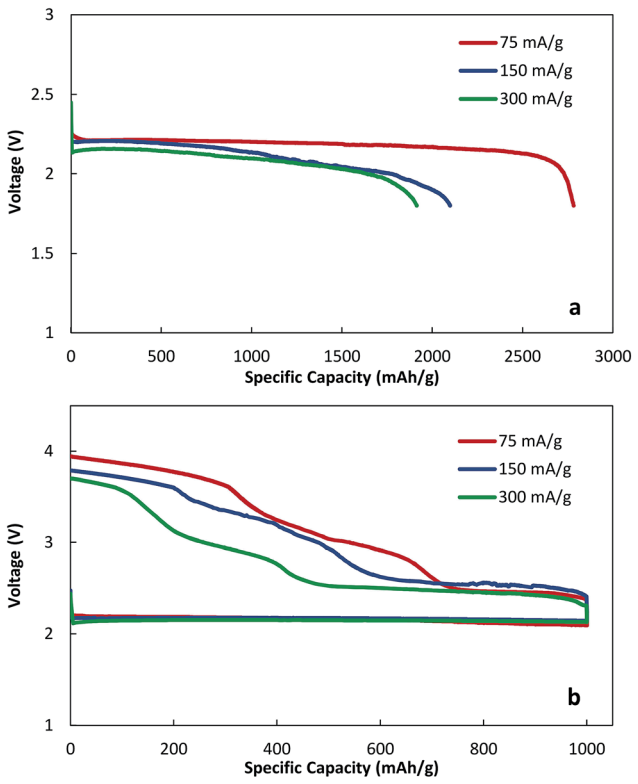

Fig. 7 Discharge curves of Na–air cells using a NH_3-treated carbon material with 85% mass loss as the cathode electrode recorded at different current densities of 75, 150 and 300 mA g^{-1} (a); limited discharge and charge curves of Na–air cells using a NH_3-treated carbon material with 85% mass loss as the cathode electrode recorded at different discharge current densities of 75, 150 and 300 mA g^{-1} and a constant charge current density of 40 mA g^{-1} (b).

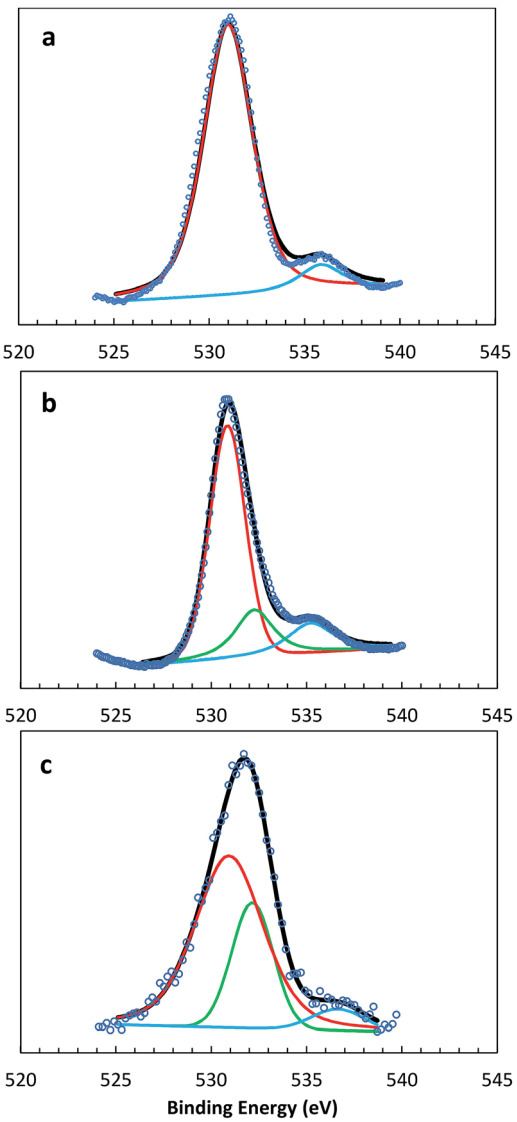

Fig. 8 Oxygen 1S spectra of reference sodium peroxide (a); and discharge products resulted at current densities of 75 (b) and 300 mA g^{-1} (c).

and also a small Auger peak around 536 eV (Na KLL).[30] The discharge product obtained from lower current densities of 75 mA g^{-1} shows a similar chemical composition consisting primarily of sodium peroxide. An additional minor fitted peak at 532.3 eV can be correlated with the deficient sodium peroxide phase ($Na_{2-x}O_2$, *vide infra*). The discharge product obtained at an elevated current density of 300 mA g^{-1} shows a broader XPS peak, indicating a wider variety of sodium oxide species. The fitted peaks at 530.9 and 532.3 eV are related to peroxide and deficient sodium peroxide species, respectively. In addition, the sodium ion Auger peak is also broader and appeared at higher binding energy which is probably a result of overlapping with the superoxide ion peak.[30] However, the discharge product obtained at an elevated current density of 300 mA g^{-1} exhibits more content of oxygen rich phases which is in accordance with charge and discharge results. The broadening clearly indicates the presence of superoxide (O_2^-), a paramagnetic species which exhibits multiplet splitting (broadening) with one unpaired electron.[31] Similar conclusion may be obtained from Na1s spectra shown in ESI Fig. S11.† In addition, XRD patterns of positive electrode materials after discharge of the cell to 1.8 V at different current densities of 75 and 300 mA g^{-1} are recorded and presented in ESI Fig. S12.† With the increase of discharge current density, the intensity of all peaks in the XRD pattern is decreased which is probably related to the formation of a "quasi-crystalline" phase of sodium oxide at higher current density. Similar behavior is also reported in the case of Li–air cells.[33]

Based on discharge curves recorded at different current densities as well as XPS results, it can be concluded that there is a competing reaction between the formation of NaO_2 and Na_2O_2, proceeding *via* eqn (1) and (2). The formation of a more thermodynamically stable peroxide ion (O_2^{2-}) at lower current densities is favorable, while the formation rate of a superoxide ion (O_2^-) is favored at higher current densities. In other words, eqn (1) is the dominant discharge reaction at higher current densities while eqn (2) is responsible for the discharge reaction at lower current densities.

To determine the effect of discharge current density on charge behaviour of Na–air batteries, cells previously discharged to a specific capacity of 1.0 Ah g^{-1} at different current densities of 75 to 300 mA g^{-1} were charged back at a constant current density of 40 mA g^{-1}. The resultant curves are shown in Fig. 7b. As the discharge current density increases from 75 to 300 mA g^{-1}, the charge capacity related to the first charge step (the decomposition of NaO_2) increases. The increase in the first charge step coupled with the observed increase in current density indicates that the formation of NaO_2 is favored at higher current densities. Recently, a computational study on the charging mechanism of Li–air cells demonstrated that the formation of an off-stoichiometric phase of $Li_{2-x}O_2$ is kinetically favorable in order to reduce the charging overpotential of the cell,[32] which has also been confirmed experimentally.[33–35] Similarly, the formation of deficient phase sodium peroxide with the general formula of $Na_{2-x}O_2$ ($0 < x < 1$) at higher discharge current densities is highly probable, especially since the oxygen-rich phase of sodium oxide (NaO_2) is more stable than lithium's counterpart.

To better understand the charge behavior, Na–air cells were subjected to discharge under different limited capacities, from 250 to 1000 mA h g^{-1}, at an elevated current density of 300 mA g^{-1} and then charged back at a constant current density of 75 mA g^{-1}. The resultant charge–discharge curves are depicted in Fig. 9a. A plateau can be observed under lower potentials while two ill-defined plateaus are observed at middle and higher potentials during the charge process of the cell discharged to 250 mA h g^{-1}. However, an increase in the discharge capacity limit from 500 to 1000 mA h g^{-1} results in a more pronounced plateau at middle and higher potentials. With an increase in discharge capacity limit the charge capacity corresponding to the lower potential plateau subsequently increases. However, an increase of discharge capacity limit also results in an increase of charge capacity corresponding to the middle and higher potential plateaus as well. The appearance of the middle and higher discharge plateaus with increasing discharge capacity limit indicates that the chemical composition of the discharge products is changing. Since the formation of NaO_2 is favorable at higher current densities, and the thermodynamic stability of Na_2O_2 is

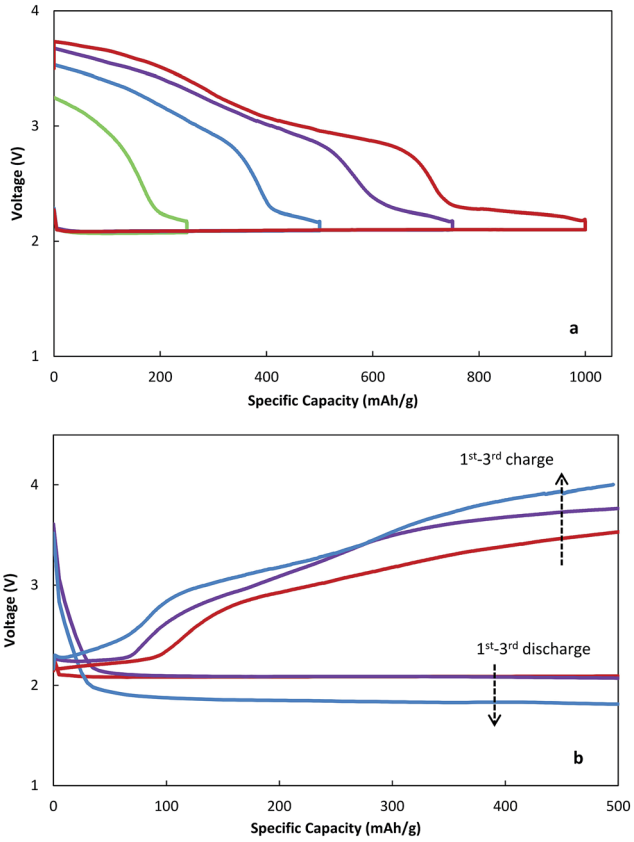

Fig. 9 Limited discharge (from 250 to 1000 mA h g^{-1}) and charge curves of Na–air cells using a NH_3-treated carbon material with 85% mass loss as the cathode electrode recorded at constant discharge and charge current densities of 300 and 75 mA g^{-1}, respectively (a); first three limited discharge and charge curves of the Na–air cell recorded at a current density of 150 mA g^{-1} (b).

higher (*vide supra*), it can be concluded that the disproportionation reaction of NaO_2 is responsible for the change in chemical composition seen for the discharge products as well as the appearance of different plateaus during the charge process. Such disproportionation reactions can be performed either chemically or electrochemically at the positive electrode *via* the following reaction mechanism:

$$2NaO_2 \rightarrow Na_2O_2 + O_2 \quad (6)$$

$$NaO_2 + (1-x)e^- + (1-x)Na^+ \rightarrow Na_{(2-x)}O_2\ (0 \leq x \leq 1) \quad (7)$$

The discharge–charge curves restricted to the low discharge capacity (250 mA h g^{-1}) can also be compared with the cyclic voltammetry (CV) curve (ESI Fig. S13†). The CV curve shows a slopping region in the cathodic cycle and two distinct peaks around 2.8 and 3.6 V in the anodic cycle related to the oxygen reduction and evolution reactions which are in accordance with discharge–charge curves, respectively. Based on the results obtained from charge–discharge curves at various current densities and different discharge capacity limits, multiple charge steps can be attributed to the decomposition reaction of different phases of sodium oxides. The lower potential charge plateau is related to a decomposition reaction of oxygen-rich phased sodium superoxide ($x \approx 1$); the middle potential charge plateau is related to the decomposition of deficient phase sodium peroxide ($0 < x < 1$); while the higher potential charge plateau is related to the decomposition of sodium-rich phased sodium peroxide ($x \approx 0$). In addition, the first three limited discharge and charge curves of the Na–air cell recorded at a current density of 150 mA g^{-1} are depicted in Fig. 9b. All consecutive cycles show complete charging with similar profiles. However, the discharge capacity starts to drop down at higher cycle numbers, mainly due to the mechanical failure of the positive electrode material as a result of binder decomposition.

The present study demonstrates the effects of discharge reaction kinetics on the chemical composition as well as charge characteristics of the Na–air battery system. The results suggest that the charge overpotential and efficiency of the cell can be controlled by modifying kinetic parameters related to the discharge reaction. The discharge process of Na–air cells at elevated current densities results in an increase of the amount of NaO_2 produced during discharge as well as decreases the charge reaction overpotential. However it also increases the chemical disproportionation reaction of NaO_2.

Similar results are also reported for the Li–air battery system. Nazar *et al.*[35] observed lower charge overpotentials for the Li–air cells discharged at higher current densities. Formation of a defective lithium peroxide phase has been mentioned to be responsible for lower charge overpotential. Further evidence toward the formation of a superoxide-like species were also reported by Zhai *et al.*[36] and Yang *et al.*,[37] indicating the existence of similar chemistry occurring between the Li– and Na–air battery systems. On the other side, more thermodynamic stability of the sodium superoxide phase leads to less activity of the discharge product of the Na–air cell toward the carbon substrate and hence results in lesser amounts of parasitic side products and lower charge overpotential in the Na–air cell which has been called "cleaner" chemistry by McCloskey *et al.*[17]

It should be also emphasized that the experimental conditions have a great influence on the chemistry of Na– and Li–air cells *via* altering the kinetic factors involving in the discharge and charge reactions of the cells. More kinetic studies are required to further understand the chemistry behind these cells and the major affecting parameters to control the chemical composition and charge overpotential of the cells.

3. Conclusion

In summary, discharge capacity, morphological changes and chemical composition of discharge products produced by a Na–air battery system have been investigated in detail and the study was based on the use of a specifically designed and heat-treated carbon material as an oxygen diffusion electrode. The specific discharge capacity of the electrode materials with varying specific surface areas demonstrated that discharge capacity is strongly dependent on electrode surface area. In addition, the result revealed that the morphology of the discharge product is also strongly dependent on surface area as well as pore size. The edge planes of the carbon substrate were proposed to serve as nucleation sites for the formation of a solid-state discharge product in the Na–air battery system. XRD, Raman, FTIR and XPS analysis of Na–air batteries indicated that both sodium peroxide and superoxide are produced during discharge cycles of the cell and decomposed at different charge steps. In addition, the formation of a deficient phase sodium peroxide ($Na_{2-x}O_2$, $0 < x < 1$) is shown to be likely. Cells discharged at different current densities also exhibited different charge profiles accompanied by a different chemical composition for the discharge product.

4. Experimental

4.1 Positive electrode material preparation

The positive electrode materials were prepared using commercial carbon black (N330). The carbon black was heat-treated under NH_3 or CO_2 (with or without H_2) atmospheres at elevated temperatures. The preparation procedure is fully described elsewhere.[19] Briefly, a precise amount of carbon black was heat-treated in a fused silica reactor under a NH_3 or CO_2 atmosphere at 1050 °C for varying durations. A small portion of the CO_2-treated samples was further pyrolysed under H_2 at 950 °C to remove oxygen containing functional groups introduced by CO_2-treatment. Heat-treatment of carbon black removes disordered graphitic structures from the carbon, producing a porous carbon structure. The amount of the carbon mass lost during the heat-treatment was measured using initial and final masses and is presented in ESI Table S1.† The SEM micrographs of N330 and heat-treated carbons (under a NH_3 atmosphere) are also shown in ESI Fig. S14.†

4.2 Physical characterizations

Morphological studies were performed by a Hitachi S-4800 field-emission scanning electron microscope (SEM) operated at 10.0 kV. N_2 adsorption/desorption isotherms were obtained using a Folio Micromeritics TriStar II Surface Area and Pore Size Analyzer. Fourier transform infra-red (FTIR) spectra and Raman scattering spectra were recorded using a Nicolet 380 and a HORIBA Scientific LabRAM HR Raman spectrometer system equipped with a 532.4 nm laser, respectively. For the FTIR measurements, the sealed testing box containing Na–air cells was moved to an argon-filled glove box (MBRUAN, with water and oxygen contents below 0.1 ppm) and the KBr disks containing 1% w/w of electrode materials were prepared in a glove box. Then, the prepared KBr disks were sealed and moved to the FTIR measurement chamber, while nitrogen gas was flushed into the chamber. For Raman analysis, the tested Na–air cells were moved to the glove box and the positive electrode materials were squeezed and sealed between two pieces of the glass slide. The Raman analysis was performed on 5 spots of the sealed samples. X-Ray diffractograms were obtained using a Bruker D8 Advance (Cu-Kα source, 40 kV, 40 mA). For the XRD measurements, the Na–air cells were moved to the glove box after testing, and the positive electrode materials of at least 4 cells were collected and placed in an air-sensitive XRD sample holder. XPS measurements were made using a glove box-equipped Omicron XM1000 X-ray tube with Al Kα source (1486.7 eV) under an operating pressure of 10^{-10} Torr. In the case of XPS measurements, positive electrodes of Na–air cells were washed with the same solvent that was used for preparing the electrolyte. Afterward, the electrodes were dried and sealed inside the glove box and then moved to the XPS place, where the samples were opened in the second glove box and directly introduced to the XPS chamber. A nickel mesh was used to correct the charging effect. The samples were only kept under a pure argon atmosphere for all analytical measurements, without any exposure to the atmospheric air.

4.3 Electrochemical measurements

Gas diffusion electrodes were prepared by casting a mixture of carbon materials and polyvinylidene fluoride (PVDF, Alfa Aesar) with a weight ratio of 9 : 1 on a separator (Celgard 3500). The electrodes were 3/8 inch in diameter with a loading capacity of ~0.25 mg. Swagelok type cells comprised of a sodium foil anode, a Celgard 3500 separator, different cathodes and a stainless steel mesh as a current collector were used to carry out electrochemical measurements. A fresh sodium foil was prepared with the aid of a homemade press machine using the sodium metal stick (from Aldrich) as a starting sodium metal inside the argon-filled glove box. The electrolyte used in this study was a 0.5 M sodium triflate ($NaSO_3CF_3$ 98%, Aldrich) dissolved in diethylene glycol diethyl ether (reagent grade ≥98%, Aldrich). Sodium triflate electrolyte salt was dried at 80 °C under vacuum for 48 hours and the water content of diethylene glycol diethyl ether solvent was removed using molecular sieves for at least 10 days. The assembled Na–air cells were placed in a homemade testing box inside the glove box and then transferred to the testing room. The argon content of the testing box was moderately vacuumed out and then pure oxygen (purity 4.3) purged into the box. The pressure of the testing box was kept at 1.0 atm during the electrochemical tests. Discharge–charge characteristics were performed using an Arbin BT-2000 battery station at room temperature (25 °C).

Acknowledgements

This research was supported by the Natural Sciences and Engineering Research Council of Canada, Canada Research Chair Program, Canada Foundation for Innovation, the University of Western Ontario and the Canadian Light Source. The authors are also indebted to Andrew Lushington for the discussion.

Notes and references

1 G. Girishkumar, B. McCloskey, A. C. Luntz, S. Swanson and W. Wilcke, *J. Phys. Chem. Lett.*, 2010, **1**, 2193–2203.
2 J. B. Goodenough and Y. Kim, *Chem. Mater.*, 2010, **22**, 587–603.
3 F. T. Wagner, B. Lakshmanan and M. F. Mathias, *J. Phys. Chem. Lett.*, 2010, **1**, 2204–2219.
4 T. Ogasawara, A. Debart, M. Holzapfel, P. Novak and P. G. Bruce, *J. Am. Chem. Soc.*, 2006, **128**, 1390–1393.
5 Y. C. Lu, B. M. Gallant, D. G. Kwabi, J. R. Harding, R. R. Mitchell, M. S. Whittingham and Y. Shao-Horn, *Energy Environ. Sci.*, 2013, **6**, 750–768.
6 A. Kraytsberg and Y. Ein-Eli, *J. Power Sources*, 2011, **196**, 886–893.
7 J. Wang, Y. Li and X. Sun, *Nano Energy*, 2013, **2**, 443–467.
8 Z. Peng, S. A. Freunberger, Y. Chen and P. G. Bruce, *Science*, 2012, **337**, 563–566.
9 Q. Sun, Y. Yang and Z. W. Fu, *Electrochem. Commun.*, 2012, **16**, 22–25.
10 W. Liu, Q. Sun, Y. Yang, J. Y. Xie and Z. W. Fu, *Chem. Commun.*, 2013, **49**, 1951–1953.
11 J. Kim, H. D. Lim, H. Gwon and K. Kang, *Phys. Chem. Chem. Phys.*, 2013, **15**, 3623–3629.
12 P. Hartmann, C. L. Bender, M. Vracar, A. Katharina Dürr, A. Garsuch, J. Janek and P. Adelhelm, *Nat. Mater.*, 2013, **12**, 228–232.
13 P. Hartmann, C. L. Bender, J. Sann, A. Katharina Dürr, M. Jansen, J. Janek and P. Adelhelm, *Phys. Chem. Chem. Phys.*, 2013, **15**, 11661–11672.
14 P. Hartmann, D. Grübl, H. Sommer, J. Janek, W. G. Bessler and P. Adelhelm, *J. Phys. Chem. C*, 2014, **118**, 1461–1471.
15 C. L. Bender, P. Hartmann, M. Vracar, P. Adelhelm and J. Janek, *Adv. Energy Mater.*, DOI: 10.1002/aenm.201301863.
16 Z. Jian, Y. Chen, F. Li, T. Zhang, C. Liu and H. Zhou, *J. Power Sources*, 2014, **251**, 466–469.
17 B. D. McCloskey, J. M. Garcia and A. C. Luntz, *J. Phys. Chem. Lett.*, 2014, **5**, 1230–1235.
18 S. Kang, Y. Mo, S. P. Ong and G. Ceder, *Nano Lett.*, 2014, **14**, 1016–1020.

19 Y. Li, X. Li, D. Geng, Y. Tang, R. Li, J. P. Dodelet, M. Lefevre and X. Sun, *Carbon*, 2013, **64**, 170–177.
20 X. Li, X. Li, M. N. Banis, B. Wang, A. Lushington, X. Cui, R. Li, T. K. Sham and X. Sun, *J. Mater. Chem. A*, 2014, **2**, 12866–12872.
21 M. Lefèvre, E. Proietti, F. Jaouen and J. P. Dodelet, *Science*, 2009, **3**, 71–74.
22 F. Jaouen and J. P. Dodelet, *J. Phys. Chem. C*, 2007, **111**, 5963–5970.
23 R. R. Mitchell, B. M. Gallant, Y. Shao-Horn and C. V. Thompson, *J. Phys. Chem. Lett.*, 2013, **4**, 1060–1064.
24 B. M. Gallant, D. G. Kwabi, R. R. Mitchell, J. Zhou, C. V. Thompson and Y. Shao-Horn, *Energy Environ. Sci.*, 2013, **6**, 2518–2528.
25 R. Black, S. Hyoung Oh, J. H. Lee, T. Yim, B. Adams and L. F. Nazar, *J. Am. Chem. Soc.*, 2012, **134**, 2902–2905.
26 R. Wen, M. Hong and H. R. Byon, *J. Am. Chem. Soc.*, 2013, **135**, 10870–10876.
27 C. E. Banks and R. G. Compton, *Analyst*, 2006, **131**, 15–21.
28 J. C. Evans, *J. Chem. Soc. D*, 1969, 682–683.
29 E. G. Brame Jr, S. Cohen, J. L. Margrave and V. W. Meloche, *J. Inorg. Nucl. Chem.*, 1957, **4**, 90–92.
30 E. Peled, D. Golodnitsky, R. Hadara, H. Mazora, M. Goora and L. Burstein, *J. Power Sources*, 2013, **244**, 771–776.
31 M. L. Shek, J. Hrbek, T. K. Sham and G. Q. Xu, *J. Vac. Sci. Technol., A*, 1991, **9**, 1640–1644.
32 S. Kang, Y. Mo, S. P. Ong and G. Ceder, *Chem. Mater.*, 2013, **25**, 3328–3336.
33 H. G. Jung, J. Hassoun, J. B. Park, Y. K. Sun and B. Scrosati, *Nat. Chem.*, 2012, **4**, 579–585.
34 H. G. Jung, H. S. Kim, J. B. Park, I. H. Oh, J. Hassoun, C. S. Yoon, B. Scrosati and Y. K. Sun, *Nano Lett.*, 2012, **12**, 4333–4335.
35 B. D. Adams, C. Radtke, R. Black, M. L. Trudeau, K. Zaghib and L. F. Nazar, *Energy Environ. Sci.*, 2013, **6**, 1772–1778.
36 D. Zhai, H. H. Wang, J. Yang, K. C. Lau, K. Li, K. Amine and L. A. Curtiss, *J. Am. Chem. Soc.*, 2013, **135**, 15364–15372.
37 J. Yang, D. Zhai, H. H. Wang, K. C. Lau, J. A. Schlueter, P. Du, D. J. Myers, Y. K. Sun, L. A. Curtiss and K. Amine, *Phys. Chem. Chem. Phys.*, 2013, **15**, 3764–3771.